PROCEEDINGS A

royalsocietypublishing.org/journal/rspa

Research

Cite this article: Metzger H, Zhang Y, Cammarano A, Prentice P. 2025 Revisiting the subharmonic route to acoustic chaos: broadband noise clearing via cavitation bubble synchronization. *Proc. R. Soc. A* **481**: 20250048. https://doi.org/10.1098/rspa.2025.0048

Received: 16 January 2025
Accepted: 20 May 2025

Subject Areas:
acoustics, computer modelling and simulation, applied mathematics

Keywords:
cavitation, subharmonic, bifurcation, broadband noise, synchronization, bubbles

Author for correspondence:
P. Prentice
e-mail: paul.prentice@glasgow.ac.uk

†These authors have contributed equally to this work and designated as co-first authors.

Electronic supplementary material is available online at https://doi.org/10.6084/m9.figshare.c.7874166.

THE ROYAL SOCIETY PUBLISHING

Revisiting the subharmonic route to acoustic chaos: broadband noise clearing via cavitation bubble synchronization

H. Metzger[1,†], Y. Zhang[1,†], A. Cammarano[2] and P. Prentice[1]

[1]Cavitation Laboratory, Centre for Medical and Industrial Ultrasonics, University of Glasgow, University Avenue, Glasgow G12 8QQ, UK
[2]Department of Aeronautics and Astronautics, University of Southampton, Burgess Road, Southampton SO16 7QF, UK

HM, 0000-0003-2662-4690; YZ, 0009-0002-0840-0482; AC , 0000-0002-8222-8150; PP, 0000-0003-2228-3622

The cavitation activity within a tube transducer subject to a linearly increasing drive amplitude is studied experimentally, via high-speed imaging and parallel acoustic detection. A spectrogram of the cavitation emission signal collected over the duration of the ramped sonication, confirms a subharmonic route to chaos; the progression from harmonic emissions to broadband noise via a period-doubling bifurcation. Stroboscopic mapping demonstrates that the emergence of broadband signal is due to increasingly asynchronous bubble collapse across the population. Particular attention is given to a region of sudden broadband clearing in the spectrogram, coincident with strong subharmonic lines, approximately halfway through the sonication. The clearing is due to phase synchronization of the bubble oscillations. Broadband noise gradually re-emerges, often with further bifurcation to include period-quadrupled emissions, as oscillations dephase again following synchronization. Numerical modelling investigates the influence of amplitude ramping, inter-bubble distance and bubble dispersity on the oscillations and emissions from a 12-bubble system, based on an experimental observation.

For a polydisperse system, it is found that a single bubble responding with period-2 oscillations initiates period-2 synchronization for the population, offering explanation for the consistent observation that prominent subharmonic emissions at half the driving frequency coincide with broadband clearing.

1. Introduction

Lauterborn & Cramer published their seminal work on the *Subharmonic Route to Chaos Observed in Acoustics*, more than 40 years ago. The paper describes the evolution of the emission signal from cavitation within a cylindrical tube transducer during a sonication of increasing drive amplitude (0–60 V, over 262 ms), figure 1, [1].

At lower voltages early in the sonication, nf_0 harmonics at integer multiples n, of the drive frequency f_0, were detected. As the voltage amplitude increased, subharmonics and ultraharmonics at $nf_0/2$ appeared [2], which Lauterborn and Cramer referred to as a period-doubling bifurcation. Further bifurcations to higher-order subharmonics $nf_0/3$, $nf_0/8$ and $nf_0/4$ were detected as the driving amplitude continued to increase.

At a threshold value of input voltage (approx. 38 V), the emission signal became dominated by broadband noise, which was termed 'acoustic turbulence' in Lauterborn and Cramer's report, although harmonic and subharmonic lines were still perceptible. On still further increasing of the drive amplitude, this acoustically chaotic system exhibited regions of 'reverse bifurcation' (approx. 52–55 V), back to period-doubled $nf_0/2$ emissions (including nf_0). Here, a reduction or clearing of broadband noise was apparent, before acoustic chaos returned at the highest amplitudes towards the end of the sonication, figure 1. Lauterborn & Koch [3] subsequently used holographic high-speed imaging to observe subharmonic oscillations of the 'whole bubble field', driven by the same (or similar) cylindrical tube transducer employed to demonstrate the subharmonic route to chaos [1].

This general trend for the development of acoustic cavitation emissions with increasing drive amplitude has since been reported for a variety of experimental configurations and ultrasonic sources; including contrast agent microbubble cavitation driven by focused ultrasound at several hundred kHz [4–7], and the cavitation at the vibrating tip of a sonotrode device, operating at 20 kHz [7]. Physically, cavitating bubbles oscillate in response to the pressure fluctuations of the driving. As the amplitude increases, the size of the bubbles (or densely packed bubble clusters) at maximum inflation, becomes sufficiently large that the inertia of the host liquid prevents collapse and shock wave generation, for every successive compressive phase of the driving. The number of compressive phases 'skipped' increases with the larger bubble sizes reached in response to higher negative pressure amplitudes [4,6,7]. These studies differ from Lauterborn and Cramer's, however, in that they employ sonications at various single-drive amplitude values, rather than a continuously increasing, or ramped amplitude sonication.

For cavitation-mediated tissue disruption and enhanced drug delivery in medical therapy, acoustic emissions are often monitored for safety and efficacy purposes [8–10]. For the specific application of blood–brain barrier opening with transcranial focused ultrasound, currently undergoing extensive clinical trials [11,12], real-time monitoring provides an active control feedback loop to avoid overtreatment [13]. In that work, 10 ms bursts of focused ultrasound at incrementally increasing pressure amplitudes (from 0.1 to 0.28 MPa, over several tens of seconds) were administered *in vivo*. The emergence of ultraharmonics (at $1.5f_0$ and $2.5f_0$) within the emission signal as the driving increased, was used as an indication that a safety threshold had been reached, following which the amplitude was reduced to some percentage value to avoid long-term irreversible damage.

It has also been shown that periodic bubble collapse shock waves [6] are responsible for many of the spectral features within the cavitation emission signal described above, for a range of ultrasonic configurations and drive frequencies [4,5,7,14]. At lower driving amplitudes,

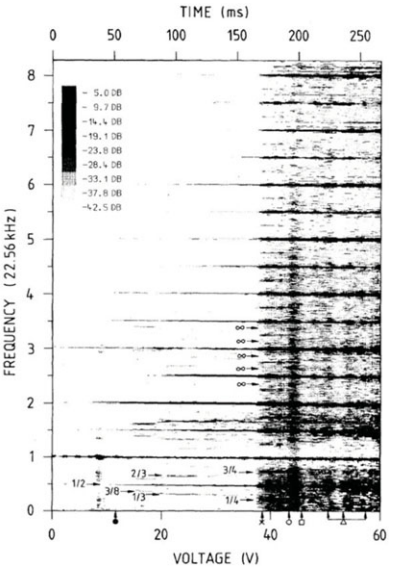

Figure 1. Lauterborn & Cramer's spectrogram [1] demonstrating the evolution of the cavitation emission signal during a sonication of increasing amplitude (0–60 V, over 262 ms). Reprinted figure with permission from [1] Copyright © (1981) by the American Physical Society.

bubble collapse shock waves with a periodicity of T_0 ($= 1/f_0$) contribute to harmonic emissions at nf_0 [4]. At higher amplitudes, period-multiplied bubble oscillations generate shock waves with periodicities of mT_0 (for $m > 1$) forming sub- and ultraharmonic emissions (nf_0/m) in the cavitation emission spectra [4,6,7]. Here, m denotes the order of period-multiplication or subharmonic response, which generally increases with the amplitude of the driving and $m - 1$ is the number of 'skipped' compressive phases, not resulting in full deflation to collapse or shock wave emission. Moreover, variations in the timings and amplitudes of shockwave emissions [4,14], and multi-fronted shockwaves from larger cavitation clusters collapsing non-uniformly [6], have been shown to constitute broadband noise, redistributing power from frequency-specific peaks to across the spectral floor. The regions of reverse bifurcation, or broadband clearing, within the noisy chaotic emissions at the higher driving amplitudes of Lauterborn and Cramer's spectrogram (figure 1, approx. 52–55 V), however, have eluded corroborated explanation.

In this study, we reconstruct Lauterborn and Cramer's experimental configuration as closely as possible, with the addition of high-speed imaging and enhanced acoustic detection, to investigate the broadband clearing phenomenon, in particular. Modelling of a multi-bubble system based on experimental observation and driven with a linearly increasing driving pressure amplitude, provides insight into the cavitation activity and the synchronization behaviour alluded to in previous studies [15,16]. Additional bifurcation analyses on excitation pressure amplitude, inter-bubble distance and bubble size deconstructs the complex dynamics into distinct mechanisms that each influence the underpinning effects.

The sections of the paper are organised as follows; first, §2 (Experimental Arrangement) is reported and sample high-speed imaging presented, followed by §3 (Theoretical Methods) along with justification for parameter selection. Post-Processing approaches applied to both the experimental and numerical data are then described §4, followed by Results from each (§5–§6), §7 (Discussion) and §8 (Conclusions).

2. Experimental arrangement

A piezoceramic tube (PZT4, F3260008, CTS Ferroperm) of 25 mm length, 40 mm inner diameter and 4 mm wall thickness was submerged in deionized water and driven at its radial resonance

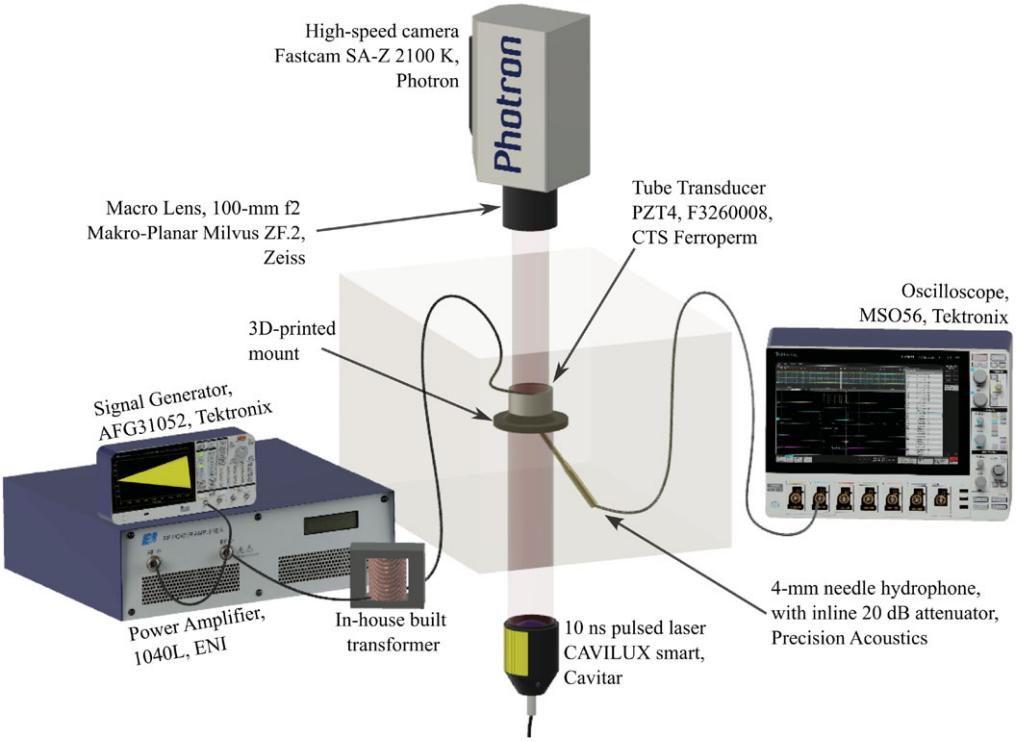

Figure 2. A schematic of the full experimental set-up, including the tube transducer and drive electronics, the high-speed imaging and illumination and the cavitation emission collection, based on a needle hydrophone.

frequency, $f_0 = 15.5$ kHz. This piezoceramic geometry results in a lower resonance than that used in Lauterborn & Cramer's study (at $f_0 = 23.56$ kHz, [1]). A custom in-house built transformer provided an electrical impedance matching network to maximize the power received by the transducer. The transducer was coated in a non-conductive resin epoxy (AbleStik 45, Loctite, USA) to ensure electrical isolation. A three-dimensional printed mount was designed such that the tube sat on a wedge to ensure consistent boundary conditions while minimizing the contact area and thus also its damping effect. The piezoceramic was excited to generate an acoustic field of increasing amplitude within the bore, over 250 ms. The tube transducer was driven with a single burst of 15.5 kHz sinusoid of linearly increasing voltage amplitude, provided by a signal generator (AFG31052, Tektronix, UK) from 0 to 450 mV peak-to-peak via a power amplifier with 55 dB gain (1040L, Electronics and Innovation, USA).

The acoustic cavitation emission signals were recorded using a 4 mm polyvinylidene fluoride needle hydrophone, with a flat sensitivity (±4 dB) of 8 V/MPa from 0.8 to 8 MHz and a lower sensitivity extending to 10 kHz, according to manufacturer specification. The hydrophone, with an inline 20 dB attenuator (Precision Acoustics, UK), transmitted the recorded data to an oscilloscope (MSO56, Tektronix, UK) at a sampling frequency of 125 MHz (a significant increase on Lauterborn & Cramer's sampling of 500 kHz [1]). The needle hydrophone was positioned 40 mm beneath the tube transducer, angled towards the geometric centre of the bore, to avoid obstructing the imaging field-of-view (FOV), as depicted in figure 2. The cavitation development over the entire sonication was captured via high-speed imaging (Fastcam SA-Z 2100 K, Photron, UK) at 80 000 frames per second, figure 3. Imaging was undertaken through a macro lens (100 mm f2 Makro-Planar Milvus ZF.2 lens, Zeiss, Germany) providing a spatial resolution of 38.5 µm per pixel. Illumination was supplied by 10 ns collimated laser pulses (CAVILUX Smart, Cavitar, Finland), synchronous to frame acquisition.

Figure 3 presents a coarse overview of the cavitation development within the bore of the tube transducer at approximately 10 ms intervals, during the ramped sonication. Clearly, a rapidly

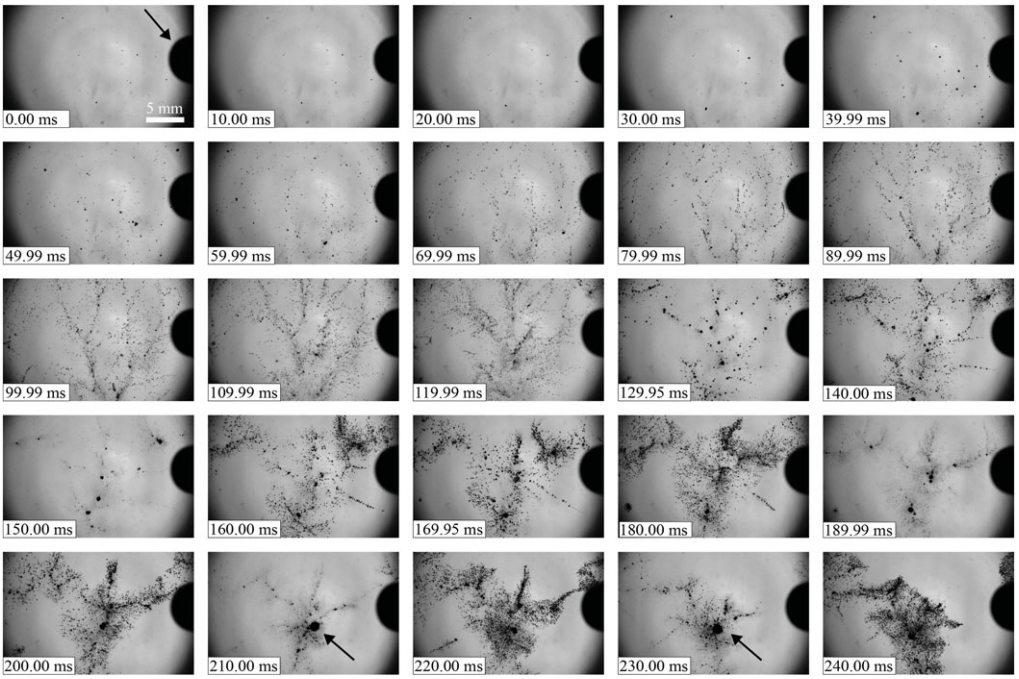

Figure 3. Representative frames at full FOV extracted from a sample high-speed image sequence captured at 80 000 frames per second, of the cavitation development over an entire 250 ms ramped sonication. The tip of the needle hydrophone, detecting the cavitation emission signal is apparent (arrowed at $t = 0.00$ ms). The central cluster of the acoustic Lichtenburg figure, which defines a region of interest (ROI), is also arrowed at 210 and 230 ms. Five millimetre scale bar provided, top-left.

developing, complex system involving many bubbles and bubble structures evolves. By 100 ms, bubbles have organized into filament structures that further develop into what is often referred to as an acoustic Lichtenburg figure [17]; a central large and densely packed cluster, most apparent in the latter stages of the sonication (arrowed at 210 and 230 ms), surrounded by dynamic bubble filaments or streamers. It is this central cluster that defines a region of interest (ROI), figure 5, which is the focus of the analysis for §5, along with the acoustic emissions collected during this sonication. A segment of the high-speed imaging sequence, available as Video 1 in the electronic supplementary material, shows the movement of bubbles along the streamers of the Lichtenberg figure.

3. Theoretical methods

Several attempts have been made to simulate multi-bubble systems with interacting bubbles, such as Lagrangian-based and Hamiltonian-based methods [18] and volume-averaged models [19]. Moreover, two-phase flow models are commonly used to study bubbly liquids, leveraging advanced numerical techniques [20]. Nigmatulin *et al.* proposed a model based on the Rayleigh–Plesset equation where a cluster of bubbles is represented as a sphere of bubbly liquid [21]. This model simplifies the problem by focusing on a single bubble, using average system parameters and disregarding interactions between bubbles. Li *et al.* furthered this work by setting up a model that contained one central cloud of bubbles, with the addition of a train of single bubbles to emulate a streamer [22,23]. Efforts have also been made to track the behaviour of each individual bubble within a multi-bubble system [24]. Recently, a unified theory for bubble dynamics, combining Rayleigh–Plesset, Gilmore and Keller-Miksis equations, has been developed and experimentally validated [25]. Although direct simulations of multi-bubble dynamics remain

computationally demanding and are typically confined to systems with a small number of bubbles, modelling multi-bubble systems with ordinary differential equations (ODEs) could reveal the bifurcation behaviour of bubbles [26].

Theoretical bubble modelling to date has used constant pressure amplitude to study steady-state behaviours. Exploring the transient behaviour of a multi-bubble system through excitation with a linearly increasing pressure amplitude has yet to be undertaken. To model the reverse bifurcation of a multi-bubble system under a ramping excitation amplitude, the model from Nasibullaeva & Akhatov [27] was extended leading to equation (3.1). Specifically, [27] uses a single second-order ODE applied to all bubbles, while in equation (3.1) separate ODEs are applied to each bubble. The model assumes spherical oscillations within an incompressible liquid, for an ideal gas at uniform pressure within each bubble, under adiabatic conditions. Heat and mass transfer across the gas–liquid interface is not accounted for. The simulations also assume stationary and non-fragmenting bubbles.

$$R_i\ddot{R}_i + \frac{3}{2}\dot{R}_i^2 = \left(1 + \frac{R_i}{c}\frac{\mathrm{d}}{\mathrm{d}t}\right)\left(\frac{P_{Li} - P_{\mathrm{amb}} - P_A}{\rho}\right) - \frac{1}{\rho}\sum_{j=1, j\neq i}^{N_b} P_{bj}, \tag{3.1}$$

where any subscript i (j) indicates the ith (jth) bubble in the multi-bubble system, R is bubble radius, $\rho = 998\,\mathrm{kg\,m^{-3}}$ is the water density, P_L is the liquid pressure acting on the bubble wall by the surrounding liquid outside the bubble, $P_{\mathrm{amb}} = 101\,\mathrm{kPa}$ is the ambient pressure, $c = 1484\,\mathrm{m\,s^{-1}}$ is the speed of sound in water. The term in equation (3.1) involving the speed of sound represents energy dissipation due to inter-bubble acoustic interactions [28]. Following the same rationale as in [27] when treating the effect of the speed of sound on the pressure terms, the bubble wall speed is negligible comparing with the speed of sound. P_b is the pressure contribution caused by the radial oscillations of all other bubbles, and P_A is the acoustic excitation pressure, which is given by equation (3.2).

$$P_A = -p_{\mathrm{amp}}\sin(2\pi f_0 t), \tag{3.2}$$

where t is time, $f_0 = 15.5\,\mathrm{kHz}$ is the excitation frequency in experiment and p_{amp} is the linearly increasing excitation pressure amplitude starting from 70 kPa with a gradient of $0.429\,\mathrm{kPa\,ms^{-1}}$. It should be noted that a ramp initiating from zero excitation pressure amplitude leads to a spectrogram dominated by nf_0 emissions at excitation amplitudes below 78.6 kPa. These are not the main focus for this study, therefore, 70 kPa was selected as the starting pressure amplitude, to skip this regime and focus on the more interesting dynamics such as the route to chaos and reverse bifurcation. Similarly, to optimize computational resources, the excitation ramp was stopped at 94.5 kPa after observing the return of acoustic chaos, as described by Lauterborn & Cramer [1] and reproduced here, experimentally.

Assuming zero mass for bubble wall and according to pressure balance, the liquid pressure, p_{Li}, at the wall of bubble i is given by equation (3.3). The bubble wall is modelled as a sharp massless interface without thickness, ensuring that the pressure balance at the interface remains valid regardless of acceleration.

$$p_{Li} = p_{gi} - \frac{2\sigma}{R_i} - \frac{4\mu\dot{R}_i}{R_i}, \tag{3.3}$$

where $\sigma = 0.072\,\mathrm{N\,m^{-1}}$ is the surface tension coefficient, $\mu = 0.001\,\mathrm{Pa\cdot s}$ is the dynamic viscosity of water and p_{gi} is the gas pressure of bubble i, which can be expressed by equation (3.4) with adiabatic law.

$$p_{gi} = \left(P_{\mathrm{amb}} + \frac{2\sigma}{R_{0i}}\right)\left(\frac{R_{0i}^3}{R_i^3}\right)^{\kappa}, \tag{3.4}$$

where $\kappa = 4/3$ is the polytropic exponent of air and R_{0i} is the equilibrium bubble radius of bubble i, indicating the amount of air contained within the bubble.

As shown in figure 4a, the spatial distribution of 12 selected bubbles observed in the high-speed imaging frame determined the locations of the bubbles used in the numerical simulation, the coordinates for which are listed in the electronic supplementary material, §S.5. Figure 4b

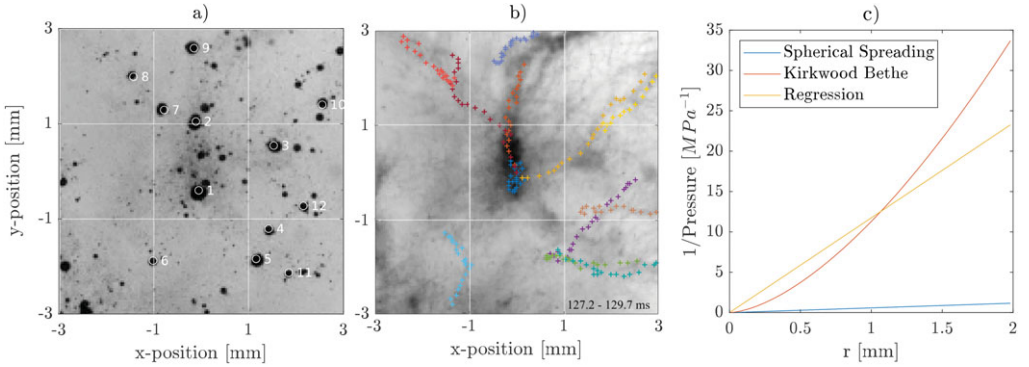

Figure 4. (a) The spatial distribution of the 12-bubble system used in the simulation was determined from the region of interest (ROI) of the high-speed imaging frame at $t = 128.7875$ ms. (b) Superpositioned frames of the bubble field captured around the time of reverse bifurcation from 127.2 to 129.7 ms, with the migration paths for each of the 12 bubbles indicated by coloured crosses (available in movie format as Video S2, electronic supplementary material). (c) The variation of the inverse of pressure emitted by a bubble in the multi-bubble system along the propagation distance.

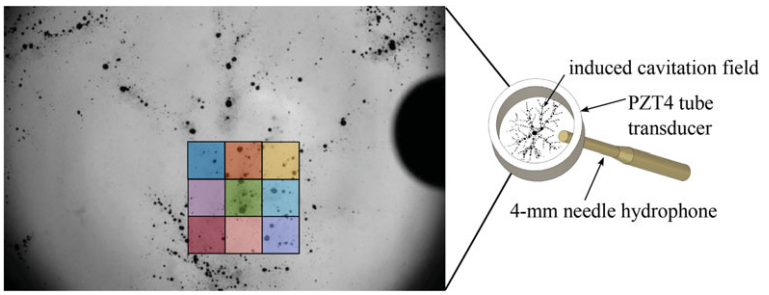

Figure 5. Schematic representation of the experiment with a representative frame of the high-speed imaging, capturing the bubble distribution at $t = 128.7875$ ms after the start of the sonication. The nine coloured boxes indicate the region of interest (ROI), with total dimensions of 6×6 mm^2, used in the stroboscopic mapping analysis.

is a superposition of high-speed imaging frames of the bubble field from 127.2 to 129.7 ms, representing the local bubble structure around the time of the reverse bifurcation phenomenon. The high-speed imaging sequence, available as Video S2 in the electronic supplementary material, shows the bubble dynamics within this structure in movie form. The sampled positions of the 12 selected bubbles are overlaid on the superposition image to show that the migration of these bubbles track the filament structures, and can therefore be taken as representative of the bubble field around the time of interest. For the purpose of the simulations, all bubbles are assumed to occupy the same two-dimensional plane throughout the sonication. The experimental observations represented by figure 7, for which the cavitation activity remains well focused within the imaging, at least for several tens of milliseconds around the moment of synchronization, would suggest this assumption is reasonable. In any case, bubble locations at varying depths along the cylindrical axis of the tube transducer, would not be expected to significantly affect the findings reported in §6. Clearly, the needle hydrophone of §2, figures 2 and 5, will detect the combined emissions from many more than just 12 bubbles. This limitation is further addressed in §§5 and 6, but a 12-bubble system is found to be sufficient for investigating the underpinning cavitation phenomenon, within reasonable computational requirements.

The computations were conducted on a dual-socket AMD EPYC 7352 system with 96 logical processors at 2.3 GHz, supported by 503 GiB of RAM, of which 486 GiB was available during the simulations. The workload was GPU-accelerated using an NVIDIA Quadro RTX 4000 with 8 GiB of memory. The system's NUMA architecture consists of two nodes, with 96 logical

processors distributed. The model involved solving equation (3.1) for the 12 bubbles with an error tolerance of 10^{-9} in MATLAB. The simulation under the ramped excitation amplitude, §6a, required approximately half an hour to complete, and the bifurcation analysis in §6b required a total computational time of approximately 300 hours for all scenarios.

The bubble pressure emission attenuates as the wave propagates. With consideration of spherical spreading loss, the pressure emission of bubbles can be described by equation (3.5) [29].

$$P_{bSS} = \frac{\rho}{r}\frac{\mathrm{d}}{\mathrm{d}t}(R^2\dot{R}) = \rho\frac{2R\dot{R}^2 + \ddot{R}R^2}{r} = \rho\left(H + \frac{1}{2}\dot{R}^2\right)\left(\frac{R}{r}\right), \tag{3.5}$$

where r is the distance from the bubble centre and $H = \ddot{R}R^2 + \frac{3}{2}\dot{R}^2$ is the difference between the ambient enthalpy and the enthalpy at the bubble wall [25]. With the Tait equation of state for water and Kirkwood–Bethe approximation, researchers have suggested that the pressure attenuation predicted by equation (3.5) is not sufficient for cavitating bubbles, and the pressure emission is given by equation (3.6) [30,31].

$$P_{bKB} = \left((p_\infty + B)\left[H\frac{(n-1)\rho_\infty}{n(p_\infty + B)} + 1\right]^{n/(n-1)} - B\right)\left(\frac{R}{r}\right)^{\alpha}, \tag{3.6}$$

where $B = 314\,\mathrm{MPa}$, $n = 7$ and $\alpha = 1.6$ are empirical parameters for water [24]. However, applied in the Kirkwood–Bethe approximation, the Tait equation of state introduces a finite variation in wave propagation speed and requires a state-dependent delay differential equation system. By contrast, assuming an incompressible liquid for wave propagation leads to an immediate interaction between bubbles, allowing for an ODE system. This significantly simplifies the system and reduces computational cost while still capturing the key bubble interaction mechanisms relevant to this study. This work seeks to find a balance between the two models. Noticing the inverse proportionality between P_{bSS} and r in the spherical spreading model, a simplification of the Kirkwood–Bethe model, equation (3.6), is obtained from the following linear regression of $1/P_{bKB}$ regarding r with a coefficient, C_p.

$$P_b = \rho\left(H + \frac{1}{2}\dot{R}^2\right)\left(\frac{R}{C_p r}\right). \tag{3.7}$$

The spherical spreading and Kirkwood–Bethe model, as shown by the blue line and red curve in figure 4c, respectively), increasingly diverge with propagation distance, r. In a multi-bubble system, bubble emissions propagate between bubbles to influence bubble behaviours. While this model accounts for pressure emissions from all bubbles, emissions from neighbouring bubbles are stronger and exert a greater influence on bubble dynamics than those from non-neighbouring ones. The largest neighbouring inter-bubble distance, as shown in figure 4a, is approximately 2 mm, and the smallest is approximately 0.3 mm. As shown in the orange line of figure 4c, the regression balances the inter-bubble distance between 0.3 and 2 mm, much better than the spherical spreading model. At the same time, it mitigates the computational strain associated with the Kirkwood–Bethe model.

To obtain an acoustic emission signal from the multi-bubble system, a virtual hydrophone is placed underneath the bubble plane, in a location equivalent to that of §2, figure 2.

4. Post-processing

To allow comparison between the experimental and numerical results, equivalent post-processing was applied to both datasets. The numerical data are non-uniformly sampled, making a conventional short-time Fourier transform (STFT) spectrogram difficult. While it is possible to enforce uniform time sampling, adaptive time-stepping is crucial to accurately resolve bubble collapse, where state variable gradients are much higher than those for other parts of the oscillation phases. Enforcing equidistant sampling or interpolating data would either lead to excessive data points or compromise the accuracy of the solution by disregarding the solver's

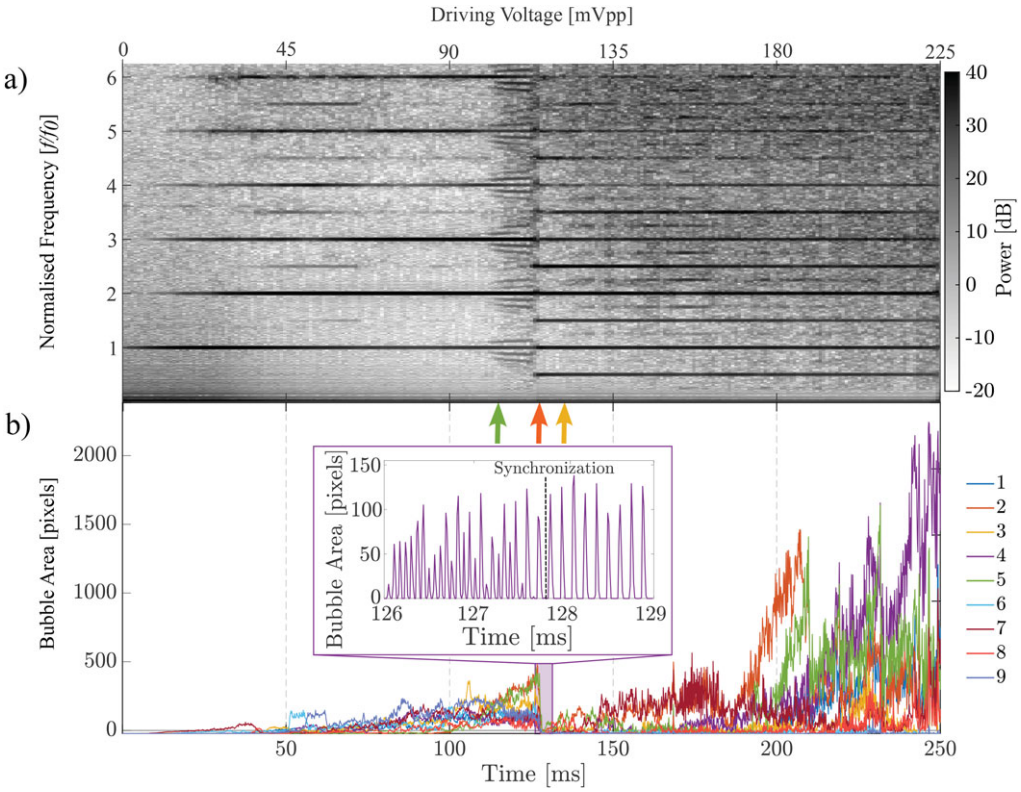

Figure 6. (a) The spectrogram of the emission signal generated by cavitation within the tube transducer, driven with a linearly increasing voltage signal, showing features comparable with Lauterborn and Cramer's results. (b) A $2T_0$ stroboscopic map of bubble area obtained from dark pixel counting within each ROI subsection, to track the degree of oscillation synchrony. Inset: the *A-t* curve of §4 indicating that the bubble oscillations transition to the period-doubled regime approximately 1 ms prior to synchronization.

optimization of time-step distribution. Resampling to a lower uniform sampling rate could result in the loss of critical spectral features in the STFT spectrogram. Without resampling, a Lomb–Scargle periodogram can directly process non-uniformly sampled data by employing a least-squares method of constructing a periodogram, using χ^2 goodness of fit calculated per frequency. For the needle hydrophone data, there are no significant discernible differences in the spectral features of interest between the spectrograms generated using short-time Fourier transforms and Lomb–Scargle periodograms. The Lomb–Scargle periodogram is compatible with uniformly sampled data and is therefore applied to both the experimental, figure 6a, and the numerical data, figure 9a, [32–34]. The spectrograms presented are generated from 200 spectra that overlap by 65%.

The selected ROI in the high-speed imaging data (as described in §2) was split into nine subsections each with dimensions of 50×50 pixels (as indicated by the coloured squares in figure 5), to analyse the relative phase of oscillation for bubbles between subsections. The subsections throughout the entire image sequence were binarized and the number of black pixels in each frame counted. The nine resulting area-time (*A-t*) curves were superimposed in a stroboscopic map [35] of period $2T_0$ to track the degree of synchrony, figure 6b. The uncertainty is determined by half the sampling intervals of the stroboscopic mapping, i.e. T_0. For the purpose of this work, the bubble oscillations are considered to be synchronized when the difference in bubble areas after $2T_0$ remains constant, within an error of 33 pixels for the experimental data. The stroboscopic map of the ROI was compared with a stroboscopic map of the whole FOV, figure S4 in the electronic supplementary material, §S.4, and therefore deemed representative

of the oscillation phases for the entire bubble population, further validating the adequacy of the chosen bubble configuration in §3. For the numerical data, which assumes spherical oscillations, the bubble area stroboscopic map was calculated from the radius–time (*R-t*) curve for each bubble, as shown in figure 9b. The bubbles are considered synchronized when the difference in bubble areas after $2T_0$ remains constant, within an error of 0.02 mm^2.

5. Experimental results

The spectrogram of the emission signal collected from the cavitation activity represented by figure 3, is presented as figure 6a. We note some variation in the feature details for each spectrogram obtained from each experimental run, with a selection presented in the electronic supplementary material, §S.1, by way of overview. We attribute these variations to the many factors that can influence how the cavitation field develops during each sonication, in particular, the initial distribution of cavitation nuclei within the tube transducer bore (which is also a function of prior sonications). Figure 6a was selected as it contains features that compare reasonably with those in Lauterborn & Cramer's spectrogram, figure 1, [1].

Figure 6a (and the spectrograms in the electronic supplementary material, §S.1, generally) shows that the cavitation field generates strong nf_0 and intermittent $nf_0/2$ emission lines during the first approximately 115 ms of the ramped sonication. As the driving voltage continues to ramp up, there is an increase in broadband noise from 115 to 128 ms (green arrow, figure 6a). This is attributable to increasingly asynchronous bubble collapse shock wave emissions from across the bubble population. Figure 7a shows the ROIs of the cavitation field, from the imaging around this stage of the sonication, at full temporal resolution (80 000 frames per second). These show that bubbles are collapsing with a periodicity close to T_0, relative to the grey dash lines, which indicate the 0.0645 ms period of the acoustic driving. Sub-millisecond variations in collapse times, however, will result in the observed redistribution of power that would otherwise be contained within nf_0 lines, to across the spectral floor [4]. This T_0-desynchronization behaviour is well captured by the growth of the stroboscopic map signal over this time interval, figure 6b. Lauterborn & Cramer termed this increase in broadband noise as acoustic turbulence/chaos and noted that it should not be sustained [1].

Within the noise, 'drifting spectral features', the frequency of which appear to vary over time, are also perceptible. These features were not apparent in Lauterborn and Cramer's spectrogram and we did not consistently observe them in the data collected for this study. We include other sample spectrograms collected under identical sonication parameters in the electronic supplementary material, §S.1, along with other investigations undertaken to interrogate these features, electronic supplementary material, §S.2 and S.3, and speculate as to their occurrence in §7.

At approximately 128 ms, there is a sudden reduction in broadband noise across all presented frequencies (red arrow, figure 6a). Frames from the high-speed imaging sequence for this part of the sonication, figure 7b, indicate that a phase synchronization (see §7 for a description, within the context of the results obtained) of the cavitation bubble and bubble cluster oscillations has occurred. The phase synchronization of the bubble population can also be observed in Video S1 of the electronic supplementary material, for the whole FOV. The stroboscopic map, figure 6b, verifies this with a sharp drop in the signal from 127.4 to 127.8 (±0.0645) ms. The synchronization of the cavitation activity is seen to occur as bubble/bubble cluster oscillations transition to period-doubled oscillations in figure 7c, relative to the T_0-grey dashed lines. The *A-t* curve of §4 in the ROI, figure 6b inset, indicates a transition into period-doubled oscillations approximately 1 ms prior to synchronization, with a corresponding emergence of strong $nf_0/2$ emission lines in the spectrogram, figure 6a.

While the cavitation emission spectrograms from equivalent sonications show that the development of spectral features can vary from sonication-to-sonication (electronic supplementary material, §S.1), the clearing of broadband noise always coincides with the emergence of strong subharmonic emissions. This could suggest that the transition to a

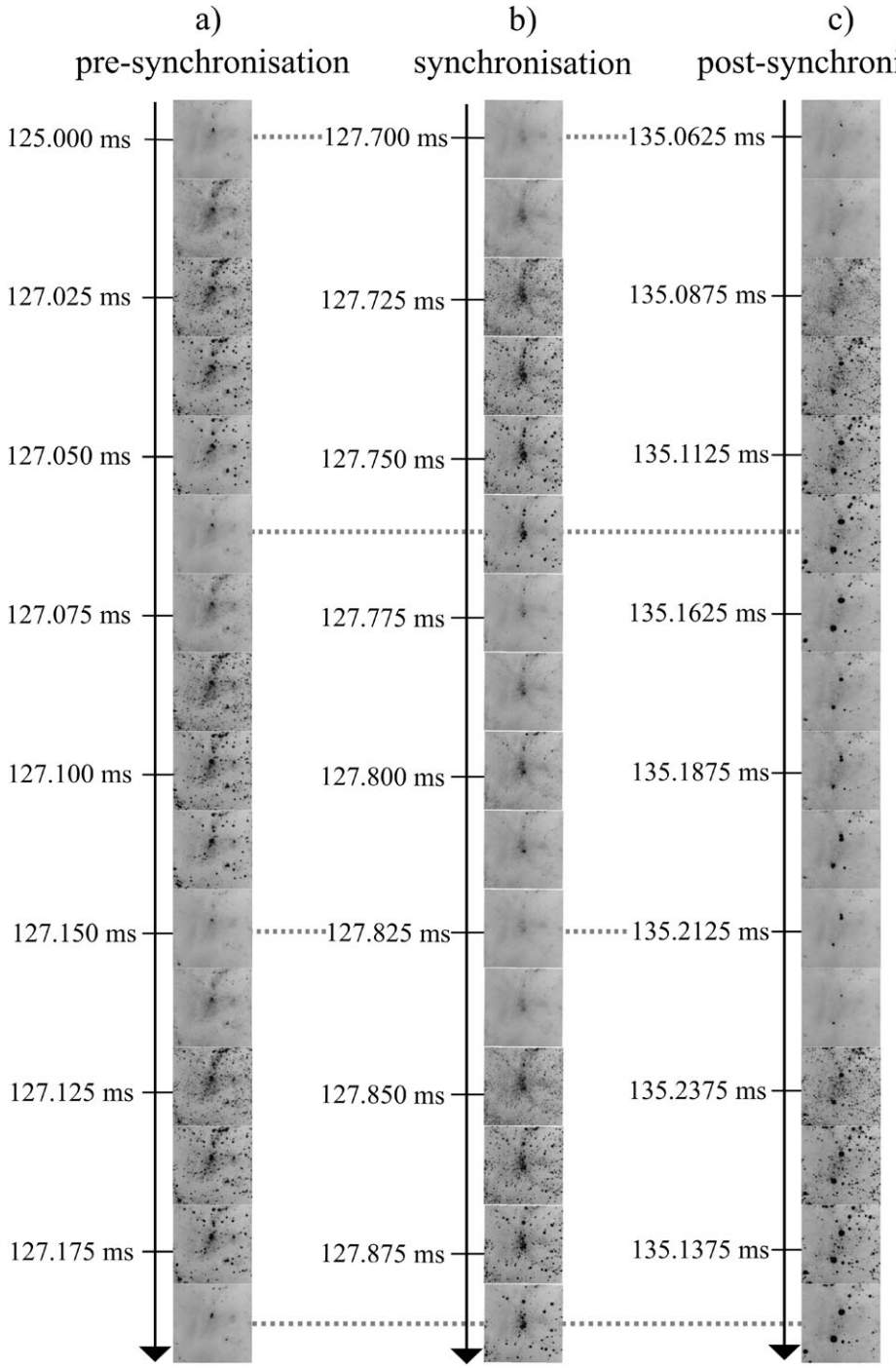

Figure 7. The region of interest (ROI) from sequential frames of the high-speed image sequence (each with dimensions of $6 \times 6\ \text{mm}^2$), (a) before synchronization of the bubbles, showing quasi-periodic oscillation at $T_0 = 0.0645$ ms, (b) during the synchronization showing the bubble clouds entering simultaneous collapses as they transition into a period-doubled regime at 127.825 ms (this section of the image sequence is also available in movie format, as Video S2 of the electronic supplementary material), (c) sometime after the synchronization event, as the synchronicity of the bubbles, responding in the period-doubled regime, has started to degrade. The grey dashed lines indicate the period of acoustic driving, $T_0 = 0.0645$ ms.

period-doubled regime creates suitable conditions under which synchronization can occur, which is investigated further in §6.

As the driving amplitude of the sonication continues to increase, the synchrony of the period-doubled oscillations is not sustained and the system starts to dephase, as previously seen for the T_0-oscillations. Figure 7c indicates that by 135 ms, dephasing of the collapse times for individual bubbles has occurred, with a corresponding 'gradual' increase in both the stroboscopic map signal, figure 6b, and the broadband emission component of the spectrogram (yellow arrow, figure 6a). Post-clearing re-emergence of the broadband signal is initially most prominent at higher frequencies, due to the sensitivity of the needle hydrophone, §2.

We have also conducted stroboscopic mapping of the cavitation activity across the full FOV (figure S.4), as detailed in the electronic supplementary material, §S.4) and verified that figure 6b is broadly representative of the entire bubble population. As well as allowing for the interpretation of the broadband noise behaviour within the spectrogram, in terms of emergence, clearing and re-emergence, this also provides some justification for limiting the numerical investigations to a 12-bubble system. Further validation may be taken from comparison of the experimental spectrogram to that generated numerically, as described in §6a.

6. Numerical results

There are limited theoretical studies investigating the synchronization effect of oscillating bubbles. In the model from Nigmatulin *et al.* [21], one ODE is necessary to model the radial oscillation of the spherical, monodisperse system, while another governs that of the individual bubbles within the system. Some numerical studies using this model [27], have compared the response of two separate monodisperse systems, each with different equilibrium radii, with a polydisperse system comprising a combination of two monodisperse systems. Nasibullaeva & Akhatov showed that oscillating bubbles in a polydisperse system collapse simultaneously, while two monodisperse systems exhibit a shift in collapse phase [27]. Tervo *et al.* confirmed this with an additional observation that if one monodisperse system exhibits period-1 oscillations while the other is in a period-doubled regime, the combined polydisperse system synchronizes to a period-doubled regime [36]. This is the only theoretical model currently available in the literature that addresses multi-bubble synchronization. However, the bubbles in the monodisperse system from this model artificially synchronize because, except for the equation of system radius, the bubble radius is modelled by only one equation. Bubbles in a monodisperse system experience different pressure contributions due to the radial oscillations of the other bubbles. This could result in significant differences in the bubble responses because of the chaotic dynamics (which is observed in bifurcation diagrams, figure 11). Therefore, the synchronization of monodisperse systems avoiding artificial synchronization, requires investigation.

This *Numerical Results* section is presented as follows; first, in §6a, a *Monodisperse System* under a ramped excitation amplitude is simulated and compared with the experimental spectrogram and stroboscopic map, figure 6. Second, in §6b, *Bifurcation Analysis* is conducted on a single bubble and the monodisperse system at four different inter-bubble distances, to explore the steady-state contribution to synchronization. Third, in §6c, a *Polydisperse System* is simulated under a ramped excitation amplitude, to investigate synchronization of different bubble sizes. Finally, the period-doubling that precedes synchronization is studied, with a further bifurcation study on equilibrium bubble radius.

(a) Monodisperse system

A monodisperse system with 12 bubbles is simulated as described in §3. The spatial distribution of the 12 bubbles is as shown in figure 4a, and the equilibrium bubble radius is $R_0 = 53.25$ μm. This selection of equilibrium bubble radius results in maximum radii of the same order as those observed experimentally according to [30], as detailed in §S.5 of the electronic supplementary material.

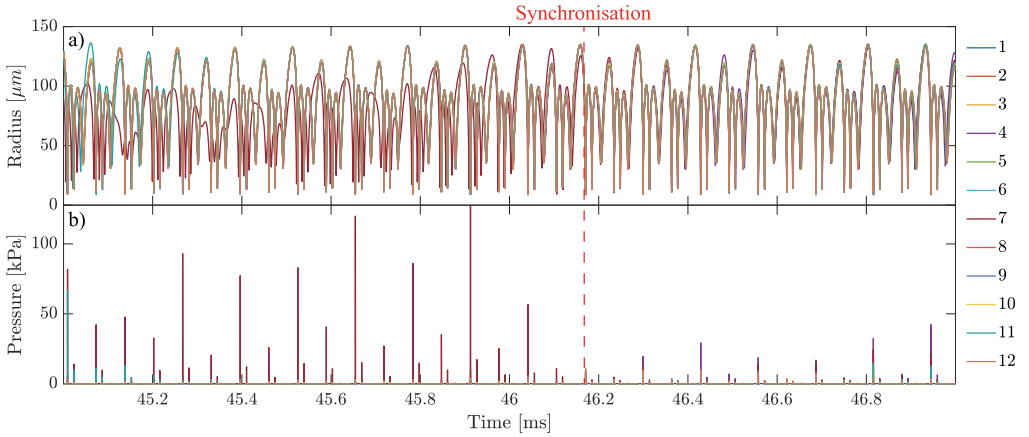

Figure 8. (a) The radial oscillation of the 12 bubbles in the numerical simulation and (b) the acoustic emissions from each bubble in the system, collected by a virtual hydrophone at an equivalent location to the needle hydrophone in the experiment.

The numerical results demonstrate bubble synchronization similar to the experimental observations. Figure 8a,b show the radial oscillations and pressure emissions of the 12 bubbles as recorded by the virtual hydrophone. Figure 8a indicates that all 12 bubbles synchronize at 46.17 ms. A study by Song *et al.* in 2019 reported the period-doubling of experimental shock wave signals [4]. Figure 8 shows that the pressure emissions before synchronization resolve into $nf_0/2$ emissions at the point of synchronization, which is the result of period-2 oscillation of the 12 bubbles.

It is important to note that the experimental signal collected by the needle hydrophone was the combined pressure signal from all the bubbles in the FOV; in this paper, a small subset of 12 bubbles is modelled. However, the spectrogram based on the combined pressure emission signal from the 12-bubble system simulation, figure 9a, shows comparable observations to the spectrogram of the experimental emission data presented in figure 6, namely the emergence, clearing and re-emergence of the broadband noise.

In figure 9a, only nf_0 emissions are present at lower amplitudes (less than 82 kPa). Broadband emissions emerge at 28.16 ms in figure 9a, due to dephasing of bubble-collapse times, as shown in figure 9c. Preceded by $nf_0/2$ emissions, a clearing of the broadband noise is shown by the *R*-*t* curve of figure 9a at 46.17 ms, which is caused by the in-phase collapsing of all the bubbles, as shown in figure 8a. Faint $nf_0/4$ emissions emerge with the post-clearing re-emergence of broadband noise in the spectrogram as bubble oscillations dephase, figure 9d at 49.68 ms.

The stroboscopic map for the numerical results, as described in §4, is presented in figure 9b. Bubbles 2 and 5 are first to synchronize with each other as their stroboscopic *A*-*t* signals become coincident at 34.17 ms. The other bubbles sequentially join the synchronized state, and the synchronization of all bubble oscillations is confirmed at 46.17 ms, where a sudden drop in the signal can be observed (marked as the red dashed line in figure 9b). This is also demonstrated by the synchronization error, obtained by the standard deviation of the stroboscopic map, as shown by the black dashed curve in figure 9b. The synchronization error in figure 9b helps to track the desynchronization, which is not easily perceived from $R-t$ or $P-t$ curves, such as figures 9d and 8. The timing of the phase synchronization coincides with the broadband clearing indicating that the 'acoustic chaos' is reduced by the synchronization of bubble oscillations, as was also observed for the experimental spectrogram and confirmed by the stroboscopic map, figure 6a,b.

(b) Bifurcation analysis

The response of a nonlinear bubble system under a ramped excitation amplitude with a constant gradient is a superposition of the transient and steady-state responses [37]. To get numerical

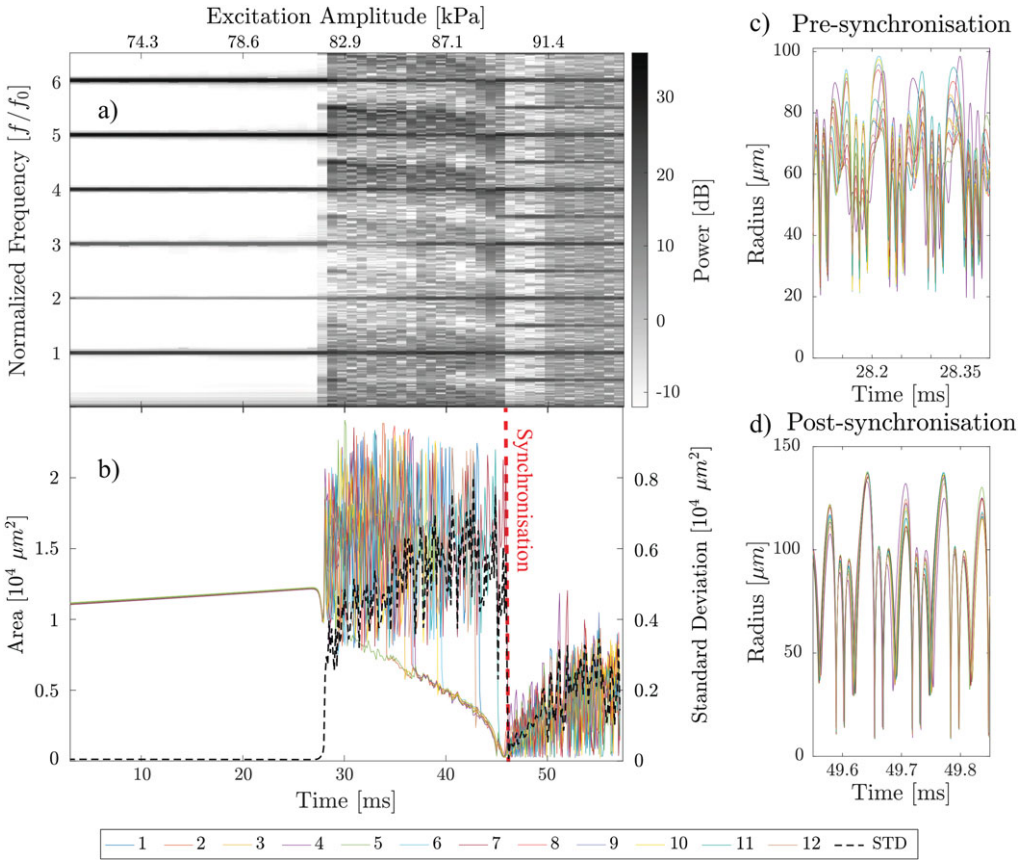

Figure 9. (a) A spectrogram of the combined emission signal collected from the 12-bubble system, by the virtual hydrophone, (b) the corresponding stroboscopic map (with period $2T_0$) of the area-time curve from the 12 bubbles, with the black dashed curve representing the standard deviation and the synchronization point marked by a red dashed line. The inset figures (c and d) on the right are the radial bubble oscillations.

insights, the contributions of transient and steady-state response should be distinguished. Transients are consistently introduced into the system response due to the ramping of the excitation amplitude. When the ramping gradient tends to zero, the excitation amplitude approaches a constant value at any given moment, effectively resembling a constant signal. In this case, the transient contribution is very small because the system amplitude of excitation is changing very gradually, and the steady-state behaviour closely approximates the system's response under this very small gradient ramping excitation. By contrast, when the excitation amplitude gradient is steep, the transient contribution becomes very prominent, leading to larger deviations from the system's steady-state behaviour. For a typical excitation ramp (with gradient between the above extremes), the excitation amplitude changes continuously, but it can be approximated with a series of incremental steps. If the steps are long enough (almost corresponding to the low-gradient case), for each step the system will settle in a steady-state response. It should be noted that true steady-state dynamics are never reached. Nonetheless, most studies focus on the steady-state behaviour because it reveals important characteristics of the system dynamics [24,38]. In this paper, the steady-state behaviour under step-increasing excitation amplitude is investigated. Each step is designed so that the steady-state response is reached and only then, the response recorded. This is essential to clarify the relation between the amplitude of excitation and the steady-state behaviour of the system. Once a clear understanding of this relation is obtained, a direct comparison with the response to a ramping signal will highlight the effect of the transient behaviour in the response.

Since the system is nonlinear, in some cases, more than one steady-state response can be achieved. Bifurcation diagrams provide a representation of all the possible solutions that the system can reach for a given level of excitation. Therefore, the bifurcation analysis will be conducted using the steady-state responses obtained under constant excitation amplitude values. Increasing excitation amplitude values were considered, with the final conditions of the state variables (i.e. bubble radius and wall speed) to the last excitation level being used as initial conditions to the next simulation. It is important to note that different initial conditions for each bubble could determine different steady-state responses; in this paper, a single set of initial conditions for each bubble is considered. Nonetheless, by characterizing the bifurcation diagrams of single and multi-bubble systems obtained in this manner, some insights to the underlying reason for bubble synchronization are gained.

(i) Single-bubble bifurcation diagram for excitation amplitude

First, the single bubble steady-state response is obtained to enable comparisons with the steady-state response of the multi-bubble system. The bifurcation analysis was done on a bubble with the same equilibrium radius ($R_0 = 53.25\,\mu m$) as that of the monodisperse system, §6a, stepping through excitation amplitudes from 70 to 95 kPa in 1125 sonications. For a given constant excitation pressure amplitude, we first identify the steady-state regime in the bubble radius–time curve. The first local maximum of the bubble radius is recorded as the initial Poincaré section. After this point, following the sampling of Poincaré section described in [39], we continue sampling one local maximum per excitation period until a total of 10 points are collected. This process is repeated for a range of excitation pressure amplitudes, allowing observation of how the bubble dynamics change, as the driving amplitude varies. Finally, a scatter plot is constructed with the excitation pressure amplitude on the x-axis and the Poincaré sections on the y-axis, forming the steady-state Poincaré plot. This plot reveals the bifurcation structure of the system, showing how steady-state bubble oscillations transition between different periodic states and chaotic behaviour as the excitation amplitude varies. As shown in figure 10a, the bubble oscillation is periodic when the excitation amplitude is below 80.4 kPa and above 84.8 kPa with a chaotic region between these two excitation levels. To verify that this response is chaotic and not simply the result of a transient behaviour, Lyapunov analysis was undertaken, an example of which (at 84.5 kPa, indicated by the orange dashed line) is shown in figure 10b. A non-negative Lyapunov exponent indicates that the bubble oscillator is exhibiting chaotic behaviour as described in [40].

(ii) Parametric analysis on inter-bubble distance

Following the single-bubble system studied in the last section, this section will focus on multi-bubble systems. In multi-bubble systems, bubble–bubble interactions need to be considered. The strength of bubble interaction increases with decreasing inter-bubble distance. Therefore, the influence of inter-bubble distance on the bifurcation diagram of the bubbles was investigated. To adjust the inter-bubble distance while preserving the relative spatial distribution of the bubbles, a scaling factor (S_F) was applied to the bubble locations shown in figure 4a. The scaling factor is a multiplier applied to the bubble centre coordinates, ensuring that the spatial configuration remains unchanged while adjusting the overall bubble spacing. Specifically, if a bubble i is originally positioned at coordinates (o_{ix}, o_{iy}), then after applying a scaling factor $S_F \neq 1$, its new position is given by $(S_F \cdot o_{ix}, S_F \cdot o_{iy})$. For this analysis, the same parameters used in the single bubble bifurcation analysis were applied to all 12 bubbles.

Figure 11 illustrates the evolution of the synchronization error under four different scaling factors. Following the post-processing procedure used in figure 9b where the synchronization error is shown as a black dashed curve, here for each steady-state response in figure 11 the synchronization error is shown.

In all four panels of figure 11, it can be observed that as the excitation amplitude increases, the synchronization error remains small due to synchronized periodic oscillations. As the

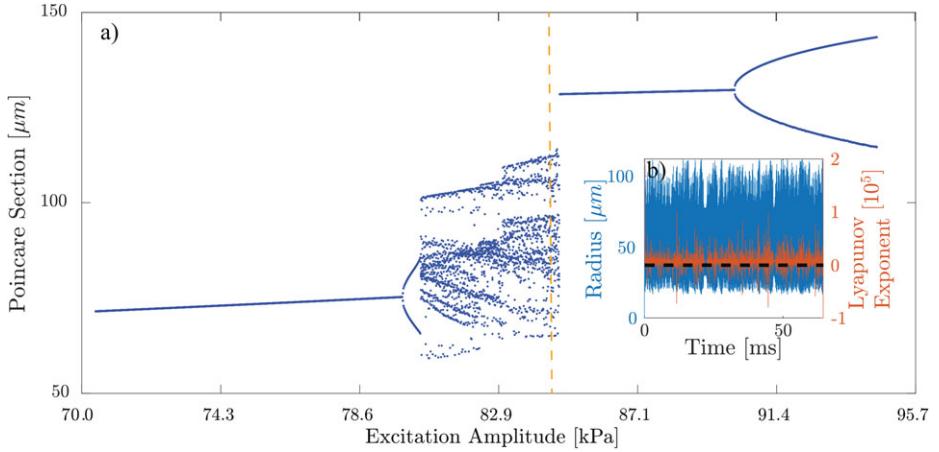

Figure 10. (a) Periodic sampling of bubble radius as Poincaré section points, plotted as a function of excitation pressure amplitude, (b) blue curve: radius–time curve at the excitation amplitude marked by the orange dashed line in (a); red curve: the maximal Lyapunov exponent calculated along the oscillation and the Lyapunov exponent value is equal to zero on the black dashed line.

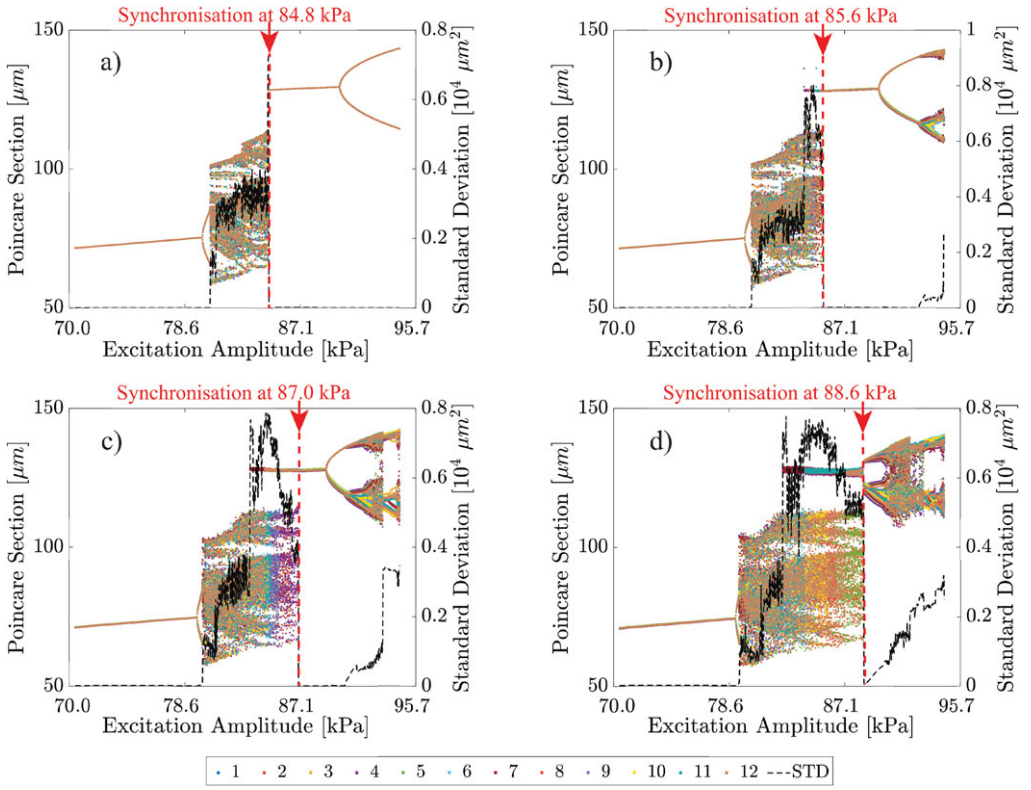

Figure 11. Excitation amplitude-dependent bifurcation structure of each bubble in the 12-bubble system at different scaling factors (S_F): (a) $S_F = 100$, (b) $S_F = 5$, (c) $S_F = 2$ and (d) $S_F = 1$. Black dashed curves: the synchronization error defined by the standard deviation of the collapsing phases.

system undergoes a period-doubling bifurcation, bubbles transition into a non-synchronized chaotic regime, causing the synchronization error to increase. The synchronization error then decreases as bubbles return to synchronized periodic oscillations at higher excitation amplitudes. In figure 11b–d, an increase in synchronization error is observed again as the system builds up non-synchronized chaotic behaviour through further period-doubling bifurcations. As the scaling factor decreases from 100 to 1 in figure 11a–d, the excitation amplitude that initiates synchronization increases, the region of period-1 after synchronization gets smaller and disappears at $S_F = 1$. On the other hand, the synchronization error increases, namely, de-synchronization occurs at lower excitation amplitude values, as S_F decreases from 100 to 1.

Figure 11 also illustrates the evolution of the bifurcation diagram; by comparing figures 11a and 10a, evident similarities in the bifurcation diagrams can be noted. This suggests that the bubble response in a multi-bubble system converges to the response of a single bubble for large inter-bubble distances, or, in other words, when the influence of the surrounding bubbles is limited. This also confirms why knowledge of the bifurcation diagram for single bubble systems is important for understanding the dynamics of multi-bubble systems.

Similarities between the synchronization errors in figures 11d and 9b, where the response to the ramped excitation amplitude is shown, indicates that the transient contribution in the ramped case is small, that is, the effect of the ramping gradient on synchronization is limited.

Finally, from figure 11d, it can be deduced that a decrease in the synchronization error only occurs if all the bubbles in the system exhibit periodic behaviour; it is sufficient that only some of the bubbles exhibit chaotic behaviour for the synchronization error to increase. This is directly related to the raising of the noise floor in the acoustic emissions, which is mentioned earlier in §5 and confirmed in §6a.

(c) Polydisperse system

Experimentally observed bubble clusters are usually polydisperse as bubble size is typically not controlled. So far, only monodisperse systems with an equilibrium radius of $R_0 = 53.25\ \mu m$ have been considered, to reduce complexity. However, it is important to determine how synchronization is affected by a polydisperse system. Using the model from Nasibullaeva & Akhatov [27], Tervo *et al.* reported that a polydisperse system can reach synchronization under a constant excitation amplitude because of bubble interaction [36]. To determine whether this is also observed under a ramped excitation amplitude, the radial bubble oscillations for three cases are simulated and compared:

— *Case A*: A single bubble with equilibrium radius of 54.3 μm (see the dashed blue curve in figure 12a).
— *Case B*: A monodisperse system of interacting bubbles with equilibrium radii of 52.5 μm (see the solid curves in figure 12a).
— *Case C*: A polydisperse system combining the bubbles from case A and case B (see figure 12b).

The same excitation ramp used for driving the monodisperse system, for the data of figure 9, is applied. The spatial distributions of the bubbles in the multi-bubble systems are the same as figure 4a. Figure 12 illustrates the radial oscillations of bubbles in the three cases A–C.

In figure 12a, the oscillations of the bubbles with different equilibrium radii are not synchronized without the interaction between the single bubble (case A) and the synchronized monodisperse system (case B). However, figure 12b demonstrates that when bubble interaction is included, the resultant polydisperse system (case C) synchronizes.

Furthermore, figure 12 shows that combining a single bubble oscillating at period-2 with a monodisperse system synchronized at period-1, results in a polydisperse system that synchronizes at period-2. This finding generalizes the work of Tervo *et al.* [36], who demonstrated a similar outcome when mixing two monodisperse systems with the same number of bubbles

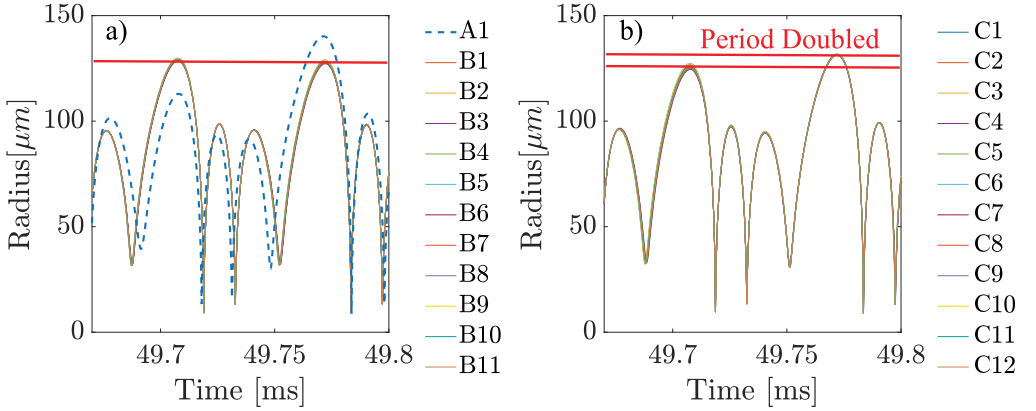

Figure 12. (a) Radius–time curves of case A: one single bubble with equilibrium radius of 54.3 µm and case B: a monodisperse multi-bubble system with equilibrium radius of 52.5 µm. (b) Radius–time curves of case C: a polydisperse multi-bubble system with $R_{01} = 54.3$ µm and $R_{0N} = 52.5$ µm ($N = 2, 3, \ldots, 12$).

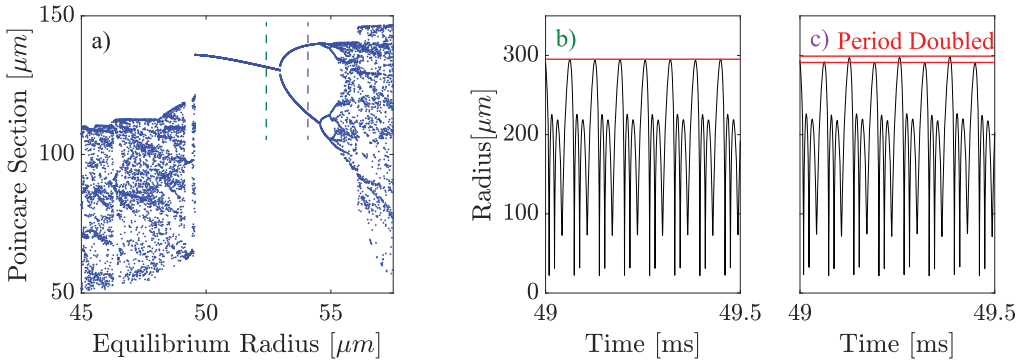

Figure 13. (a) Bifurcation diagram for equilibrium bubble radius (R_0) at an excitation amplitude of 91 kPa, where the single bubble radius is sampled every forcing cycle. Green dashed line: $R_0 = 52.5$ µm, purple dashed line: $R_0 = 54.3$ µm. (b) Radius–time curves of a monodisperse system with equilibrium radius of 52.5 µm. (c) Radius–time curves of a polydisperse multi-bubble system with $R_{01} = 54.3$ µm and $R_{0N} = 52.5$ µm ($N = 2, 3, \ldots, 12$).

synchronized at period-1 and period-2, respectively. Although a monodisperse system can be synchronized at period-1 after the chaotic region, as demonstrated in case B, the experimental observations of figure 6a, indicate period-doubling at the onset of broadband noise clearing. This could be explained by the polydispersity of experimental bubble systems, which is further explored in a bifurcation analysis conducted using the equilibrium radius as the free parameter, i.e. the changing parameter in the bifurcation diagram. Considering the close relation existing between the bifurcation diagram of a monodisperse system and a single bubble system, this analysis is carried out considering a single bubble system.

Figure 13a shows the bifurcation diagram for the equilibrium bubble radius with the excitation amplitude of 91 kPa. This corresponds to 49 ms in the ramping case, figure 13b,c, for which the same excitation ramp as described in §3 was applied. The bubble radius is plotted as Poincaré sections for 10 consecutive forcing periods. In total, 1391 equilibrium radii were uniformly sampled in the vicinity of 53.25 µm. As seen in figure 13a, the bubbles with $R_0 = 52.5$ µm (green dashed line) and $R_0 = 54.3$ µm (purple dashed line) are responding with period-1 and period-doubled oscillations, respectively.

Case B shows an 11-bubble monodisperse system, while figure 13b presents a 12-bubble monodisperse system. Figure 13c illustrates the corresponding 12-bubble polydisperse system from case C. In figure 13b, all bubbles have an equilibrium radius of 52.5 µm, corresponding to

the green dashed line in figure 13a. To introduce polydispersity into this initially monodisperse system, bubble 1 is given an equilibrium radius of 54.3 µm, corresponding to the purple dashed line in figure 13a, while bubbles 2–12 retain an equilibrium radius of 52.5. This distinction is visually indicated in figures 13b,c, where the figure labels (b) and (c) are coloured green and purple, respectively, matching the dashed lines in figure 13a. The spatial distributions of bubbles in both systems are the same as figure 4a. The resulting bubble oscillations are shown in figure 13b,c, where the black curve is the equivalent radius calculated by taking the third-order root of the summation of the volume of all bubbles, at a specific time during oscillation, i.e. $R_{\text{sum}} = \sqrt[3]{R_1^3 + R_2^3 + R_3^3 + \ldots + R_{12}^3}$, for consistency with the dark pixel calculation used in the experimental post-processing which is also an integral measure from several bubbles. As shown in figure 13a, a bubble with an equilibrium radius of 52.5 µm oscillates with period-1, while a bubble with an equilibrium radius of 54.3 µm oscillates with period-2. Therefore, by modifying the size of a single bubble from 52.5 to 54.3 µm within the monodisperse system, figure 13b, we investigate the impact of this period doubling bubble on the oscillation period of the new polydisperse system, figure 13c. Figure 13b shows the monodisperse system synchronizes at period-1. Figure 13c, however, shows the synchronized polydisperse system with overall period-2 oscillations. This illustrates that the existence of only one period-doubled bubble (namely the 54.3 µm bubble) can result in the period-doubled synchronization of a polydisperse system. Experimentally, the system is always polydisperse. Bubbles with a range of equilibrium radii that allow for periodic responses can synchronize, and even if only some have a period-2 oscillation, this will result in a combined response that shows period-doubled oscillations.

7. Discussion

The main experimental finding of this study is that synchronization of bubble and bubble cluster oscillations within a cavitating population driven by an acoustic field of linearly ramped amplitude, causes a sudden reduction in the broadband emissions generated by the population. Stroboscopic mapping measures the synchrony of bubble oscillations across subsections of a selected ROI from the high-speed imaging of the cavitation activity, for the duration of the sonication. This confirms that the rise in broadband emissions is attributable to dephasing of initial T_0 oscillations (with associated nf_0 emissions) across the bubble population. The moment of broadband clearing in the hydrophone detection coincides with a marked drop in the stroboscopic map signal, with cavitating bubbles synchronizing to period-doubled oscillations, apparent in the imaging and preceded by strong emissions at $nf_0/2$ in the spectrogram that are sustained for the remaining duration of the sonication.

The numerical results suggest that the synchronization of the entire bubble population is observed only when all bubbles are responding periodically; leading to the conclusion that just a few bubbles exhibiting chaotic behaviour is enough to result in a high synchronization error. For a polydisperse system, it is also shown that bubble interaction can result in synchronization between bubbles with different equilibrium radii, and that a period-doubled response of some bubbles can trigger synchronization to period-2 oscillations across the population. These findings are consistent with the experimental observation that strong $nf_0/2$ spectral lines precede the broadband clearing, in all experimental spectrograms (in figure 6, see the spectrogram between 127.6 and 128 ms, and in §S.1 in the electronic supplementary material, figures S.1(a–d), and the spectrogram of Lauterborn & Cramer [1]). The $nf_0/2$ spectral lines that are observed in the region 30–75 ms in figure 6a—well before the increase in broadband noise—do not coincide with broadband clearing, suggesting that transition between period-1 and period-2 is possible even without passing through regions characterized by high broadband noise. This suggests that the signal remains periodic during this transition.

Specifically, we have observed phase synchronization, described as the state that occurs when individual oscillators within a population, shift in frequency to oscillate in phase with each other, rather than complete synchronization, where phases of the oscillators align with

identical amplitude [35]. Synchronization phenomena occur when individual oscillators are coupled within a system, often in a way that allows energy transfer between the oscillators, such as metronomes or inverted pendula that are coupled via a freely moving base [41] and the natural pace making of the heart, which uses electrical signals emitted by the sinoatrial node to synchronize the contraction of the heart muscles [42]. For the bubble synchronization investigated in this study, the numerical simulations of monodisperse and polydisperse system indicate that the coupling between bubbles leads to synchronization and therefore results in the mechanism of bubble interaction via their pressure emissions. When one bubble oscillates, it emits pressure waves that influence surrounding bubbles, altering their oscillatory behaviour. The physical reason why this coupling results in synchronization is demonstrated in the work of Tervo *et al.* [36], where it was shown that coupling shifts the timing of bubble collapse, aligning them to occur in-phase. This mechanism is reproduced in this study where the phase alignment stabilizes over time, leading to the observed synchronization.

Synchronization can also occur via non-physical interactions, with coupling mediated by social or communal factors, for example, the synchronous flashing of male fireflies via the light pulses from all other insects in the population as a courtship signal [43]. Another example, with some similarities to the cavitation emission signal development described here, was found in the applause of an audience following opera/theatre performances [44]. After a few seconds of initially 'tumultuous' and incoherent clapping, a synchronization to period-doubled clapping was reported. Here, the coupling is mediated by an audience-level desire to express its appreciation by maximizing the average noise intensity of its applause. Interestingly, period-doubling was found to be a condition for synchronizing, with the slower clapping reducing the clap frequency distribution or dispersion, allowing synchronization to occur. The authors also noted that synchronization is not sustained, the desire for increased clapping intensity reduces the clapping period, which dephases the period-doubled clapping back to the faster asynchronous clapping. The resulting conflict between increased intensity and synchronization generates a sequence of synchronized and desynchronized regimes.

As noted in §5, what we have termed drifting spectral features within the pre-clearing broadband noise of the spectrogram, figure 6a, are not apparent within Lauterborn and Cramer's original spectrogram. They did note, however, that *single lines may visibly oscillate* [1], which although not described further, may have been in reference to comparable observations. In the electronic supplementary material, initial results from several attempts to further investigate these features are presented, in addition to the other experimental spectrograms which show that they were not reliably generated. These include filtering and down-sampling of the data of figure 6a in accordance with Lauterborn and Cramer's report, electronic supplementary material, §S2. This reprocessing is seen to considerably suppress the appearance of the drifting features in our spectrogram. Moreover, spectrograms from 'ramp-to-plateau' sonications are presented, electronic supplementary material, §S.3, for which the amplitude was ramped up to voltage values within the pre-clearing broadband noise emergence, and thereafter held constant, electronic supplementary material, §S.3. These results indicate that the drifting features stabilize to a constant frequency value, for the plateau phase of the sonication. While further investigations are required to substantiate the mechanism responsible for these features, we would suggest that they originate from individual bubbles responding to the transient nature of the ramped excitation amplitude.

One application where cavitation synchronization may be an important consideration is that of blood–brain barrier opening, in medical therapy. Here, many contrast microbubbles distributed throughout that vasculature of the brain, are subjected to an effectively ramped sonication, as described in §1. Although sub- and/or ultra-harmonics can be monitored for safety purposes [10,45], cavitation dose, for which emissions are integrated over some bandwidth, can also be used as a metric for determining optimal treatment duration [46,47]. Microbubble-cavitation synchronization during the focused ultrasound sonication would therefore be expected to result in an otherwise unexpected reduction of the signal being monitored. For a real-time control feedback loop modulating the intensity of the driving through monitoring of broadband emission

components, an algorithm may further increase the driving to compensate for the perceived reduction in the level of cavitation activity. We note, however, that broadband re-emergence following the synchronization event observed experimentally, occurs within a few tens of acoustic cycles and therefore may not be a significant concern.

Another application where cavitation synchronization may occur is that of acoustic cleaning, where the amplitude of the driving is often modulated at 50 or 100 Hz, such that the cavitation is driven by a time-varying, or ramping, intensity [48]. Indeed, there are reports of cavitation activity in cleaning bath-type configurations, with observations of bubble structures oscillating subharmonically, both in and out of phase with each other [49,50], along with associated subharmonic acoustic emissions [50,51]. In the current work, we demonstrate bubble oscillation phase synchronization within the population of a cavitation structure, mediated by interactions between the cavitating bubbles of that structure, associated clearing of broadband emissions and the role of period-doubled oscillations in generating favourable conditions for synchronization to occur.

8. Conclusion

This study presents a comprehensive investigation into the dynamics of bubble synchronization in a cavitating system, leveraging experimental and numerical approaches to explore how synchronization phenomena influence the acoustic emissions. Through the use of stroboscopic mapping and spectrogram analysis, we have identified and characterized the transitions between synchronized and desynchronized states. These transitions are marked by notable acoustic features, including the clearing and re-emergence of broadband noise, revealing the intricate interplay between bubble oscillation dynamics and acoustic emissions.

Our numerical simulations, based on an extension of the Nasibullaeva & Akhatov model [27], demonstrate agreement with experimental observations, providing a robust framework for modelling multi-bubble systems under ramped excitation. Importantly, the bifurcation analysis highlights how system parameters, such as inter-bubble distance and equilibrium radius, influence the synchronization behaviour, leading to distinct regimes of stability and instability. These findings offer a detailed understanding of the underlying mechanisms driving synchronization and their sensitivity to system properties.

The insights gained in this study have broad implications for cavitation-based applications. By elucidating the conditions that promote synchronization, this work paves the way for enhanced control strategies in technologies where cavitation plays a pivotal role, including therapeutic ultrasound, sonochemistry and industrial cleaning. For instance, the ability to manipulate synchronization dynamics could enable more precise targeting in medical treatments or improve energy efficiency in chemical processing.

Future work should extend the current findings by addressing limitations in the modelling framework. Incorporating bubble migration, liquid compressibility, coalescence and fragmentation, non-spherical oscillations, higher-order hydrodynamic effects, a more representative number of oscillating bubbles, and environmental factors such as dissolved gas concentrations and temperature will be needed for refining the predictive capabilities of numerical models. Heat and mass transfer in bubbles can also be incorporated. The numerical method proposed by [52] models the processes of heat and mass transfer while accounting for phase change and liquid compressibility. In addition, investigating the impact of more complex excitation waveforms, such as modulated or pulsed signals, may uncover new pathways for controlling cavitation dynamics.

In conclusion, this study provides a critical step forward in understanding bubble synchronization and its influence on cavitation phenomena. By bridging experimental and numerical methods, we have established a foundation for future research and innovation in the control and application of cavitation. The methodologies and findings presented here hold promise for advancing both scientific understanding and technological development across a range of fields.

Data accessibility. Supplementary material is available online [53], and data are available at the following repository: [54].

The data are provided in the electronic supplementary material [53].

Declaration of AI use. We have not used AI-assisted technologies in creating this article.

Authors' contributions. H.M.: data curation, formal analysis, investigation, methodology, validation, visualization, writing—original draft, writing—review and editing; Y.Z.: data curation, formal analysis, investigation, methodology, validation, visualization, writing—original draft, writing—review and editing; A.C.: funding acquisition, investigation, methodology, supervision, writing—original draft, writing—review and editing; P.P.: conceptualization, funding acquisition, investigation, methodology, supervision, writing—original draft, writing—review and editing.

All authors gave final approval for publication and agreed to be held accountable for the work performed therein.

Conflict of interest declaration. We declare we have no competing interests.

Funding. We acknowledge funding from the UK Engineering and Physical Sciences Research Council (EPSRC, grant nos. EP/W018632/1 and EP/V036777/1), Innovate UK program (grant no. 10125993), EU (grant agreement ID 101122277) and the UKRI REACT project. H.M. is supported by the FUSE CDT (grant no. EP/S023879/1), funded by EPSRC.

Acknowledgements. The authors are grateful for support from A. Feeney and A. Abbott, and to P. Daly for tube transducer fabrication. We also thank the American Physical Society for granting permission for the use of figure 1 [1] for this publication.

References

1. Lauterborn W, Cramer E. 1981 Subharmonic route to chaos observed in acoustics. *Phys. Rev. Lett.* **47**, 1445. (doi:10.1103/PhysRevLett.47.1445)
2. Esche R. 1952 Untersuchung der schwingungskavitation in flüssigkeiten. *Acta Acust. United with Acust.* **2**, 208–218.
3. Lauterborn W, Koch A. 1987 Holographic observation of period-doubled and chaotic bubble oscillations in acoustic cavitation. *Phys. Rev. A* **35**, 1974. (doi:10.1103/PhysRevA.35.1974)
4. Song JH, Moldovan A, Prentice P. 2019 Non-linear acoustic emissions from therapeutically driven contrast agent microbubbles. *Ultrasound Med. Biol.* **45**, 2188–2204. (doi:10.1016/j.ultrasmedbio.2019.04.005)
5. Gümmer J, Schenke S, Denner F. 2021 Modelling lipid-coated microbubbles in focused ultrasound applications at subresonance frequencies. *Ultrasound Med. Biol.* **47**, 2958–2979. (doi:10.1016/j.ultrasmedbio.2021.06.012)
6. Song JH, Johansen K, Prentice P. 2016 An analysis of the acoustic cavitation noise spectrum: the role of periodic shock waves. *J. Acoust. Soc. Am.* **140**, 2494–2505. (doi:10.1121/1.4964633)
7. Yusuf L, Symes MD, Prentice P. 2021 Characterising the cavitation activity generated by an ultrasonic horn at varying tip-vibration amplitudes. *Ultrason. Sonochem.* **70**, 105273. (doi:10.1016/j.ultsonch.2020.105273)
8. Tung YS, Vlachos F, Choi JJ, Deffieux T, Selert K, Konofagou EE. 2010 *In vivo* transcranial cavitation threshold detection during ultrasound-induced blood–brain barrier opening in mice. *Phys. Med. Biol.* **55**, 6141–6155. (doi:10.1088/0031-9155/55/20/007)
9. Arvanitis CD, Livingstone MS, Vykhodtseva N, McDannold N. 2012 Controlled ultrasound-induced blood-brain barrier disruption using passive acoustic emissions monitoring. *PLoS ONE* **7**, e45783. (doi:10.1371/journal.pone.0045783)
10. McDannold N, Zhang Y, Supko JG, Power C, Sun T, Peng C, Vykhodtseva N, Golby AJ, Reardon DA. 2019 Acoustic feedback enables safe and reliable carboplatin delivery across the blood-brain barrier with a clinical focused ultrasound system and improves survival in a rat glioma model. *Theranostics* **9**, 6284–6299. (doi:10.7150/thno.35892)
11. McDannold N, Wen PY, Reardon DA, Fletcher SM, Golby AJ. 2024 Cavitation monitoring, treatment strategy, and acoustic simulations of focused ultrasound blood-brain barrier disruption in patients with glioblastoma. *J. Control. Release* **372**, 194–208. (doi:10.1016/j.jconrel.2024.06.036)
12. Farzad Maroufi S, Sadegh Fallahi M, Parmis Maroufi S, Sheehan JP. 2024 Focused ultrasound blood-brain barrier disruption in high-grade gliomas: scoping review of clinical studies. *J. Clinical Neurosci.* **128**, 110786. (doi:10.1016/j.jocn.2024.110786)

13. O'Reilly MA, Hynynen K. 2012 Blood-brain barrier: real-time feedback-controlled focused ultrasound disruption by using an acoustic emissions–based controller. *Radiology* **263**, 96–106. (doi:10.1148/radiol.11111417)
14. Yasui K. 2023 Origin of the broad-band noise in acoustic cavitation. *Ultrason. Sonochem.* **93**, 106276. (doi:10.1016/j.ultsonch.2022.106276)
15. Parlitz U, Mettin R, Luther S, Akhatov I, Voss M, Lauterborn W. 1999 Spatio–temporal dynamics of acoustic cavitation bubble clouds. *Phil. Trans. R. Soc. Lond. A* **357**, 313–334. (doi:10.1098/rsta.1999.0329)
16. Ohl CD, Kurz T, Geisler R, Lindau O, Lauterborn W. 1999 Bubble dynamics, shock waves and sonoluminescence. *Phil. Trans. R. Soc. Lond. A* **357**, 269–294. (doi:10.1098/rsta.1999.0327)
17. Akhatov I, Parlitz U, Lauterborn W. 1994 Pattern formation in acoustic cavitation. *J. Acoust. Soc. Am.* **96**, 3627–3635. (doi:10.1121/1.410580)
18. Ilinskii YA, Hamilton MF, Zabolotskaya EA. 2007 Bubble interaction dynamics in Lagrangian and Hamiltonian mechanics. *J. Acoust. Soc. Am.* **121**, 786–795. (doi:10.1121/1.2404798)
19. Fuster D, Colonius T. 2011 Modelling bubble clusters in compressible liquids. *J. Fluid Mech.* **688**, 352–389. (doi:10.1017/jfm.2011.380)
20. d'Agostino L, Brennen CE. 1989 Linearized dynamics of spherical bubble clouds. *J. Fluid Mech.* **199**, 155–176. (doi:10.1017/S0022112089000339)
21. Nigmatulin R, Akhatov IS, Vakhitova N, Nasibullayeva ES. 2000 Dynamics of bubble clusters. *Am. Inst. Phys.* **524**, 455–458. (doi:10.1063/1.1309263)
22. Li F, Zhang X, Tian H, Hu J, Chen S, Mo R, Wang C, Guo J. 2022 Interactions of bubbles in acoustic Lichtenberg figure. *Ultrason. Sonochem.* **87**, 106057. (doi:10.1016/j.ultsonch.2022.106057)
23. Li F, Huang C, Zhang X, Wang C, Guo J, Lin S, Shen Z, Tian H. 2023 Structure of bubble cluster adjacent to the water surface in the ultrasonic field. *Ultrasonics* **132**, 106992. (doi:10.1016/j.ultras.2023.106992)
24. Haghi H, Sojahrood A, Kolios MC. 2019 Collective nonlinear behavior of interacting polydisperse microbubble clusters. *Ultrason. Sonochem.* **58**, 104708. (doi:10.1016/j.ultsonch.2019.104708)
25. Zhang A, Li SM, Cui P, Li S, Liu YL. 2023 A unified theory for bubble dynamics. *Phys. Fluids* **35**, 033323. (doi:10.1063/5.0145415)
26. Chong K, Quek C, Dzaharudin F, Ooi A, Manasseh R. 2010 The effects of coupling and bubble size on the dynamical-systems behaviour of a small cluster of microbubbles. *J. Sound Vib.* **329**, 687–699. (doi:10.1016/j.jsv.2009.09.037)
27. Nasibullaeva S, Akhatov IS. 2005 Dynamics of a bubble cluster in an acoustic field. *Acoust. Phys.* **51**, 705–712. (doi:10.1134/1.2130902)
28. Nasibullaeva ES, Akhatov I. 2013 Bubble cluster dynamics in an acoustic field. *J. Acoust. Soc. Am.* **133**, 3727–3738. (doi:10.1121/1.4802906)
29. Mettin R, Akhatov I, Parlitz U, Ohl C, Lauterborn W. 1997 Bjerknes forces between small cavitation bubbles in a strong acoustic field. *Phys. Rev. E* **56**, 2924. (doi:10.1103/PhysRevE.56.2924)
30. Liang XX, Linz N, Freidank S, Paltauf G, Vogel A. 2022 Comprehensive analysis of spherical bubble oscillations and shock wave emission in laser-induced cavitation. *J. Fluid Mech.* **940**, A5. (doi:10.1017/jfm.2022.202)
31. Denner F, Schenke S. 2023 Modeling acoustic emissions and shock formation of cavitation bubbles. *Phys. Fluids* **35**, 012114. (doi:10.1063/5.0131930)
32. Lomb NR. 1976 Least-squares frequency analysis of unequally spaced data. *Astrophys. Space Sci.* **39**, 447–462. (doi:10.1007/BF00648343)
33. Scargle JD. 1982 Studies in astronomical time series analysis. II-Statistical aspects of spectral analysis of unevenly spaced data. *Astrophys. J.* **263**, 835–853. (doi:10.1086/160554)
34. VanderPlas JT. 2018 Understanding the lomb–scargle periodogram. *Astrophys. J. Suppl. Ser.* **236**, 16. (doi:10.3847/1538-4365/aab766)
35. Rosenblum M, Kurths J. 2003 *Synchronization: a universal concept in nonlinear science*. Cambridge, UK: Cambridge University Press.
36. Tervo JT, Mettin R, Lauterborn W. 2006 Bubble cluster dynamics in acoustic cavitation. *Acta Acustica United with Acustica* **92**, 178–180.
37. Leighton T. 2012 *The acoustic bubble*. New York, NY: Academic Press.
38. Hegedüs F. 2014 Stable bubble oscillations beyond Blake's critical threshold. *Ultrasonics* **54**, 1113–1121. (doi:10.1016/j.ultras.2014.01.006)

39. Parlitz U, Englisch V, Scheffczyk C, Lauterborn W. 1990 Bifurcation structure of bubble oscillators. *J. Acoust. Soc. Am.* **88**, 1061–1077. (doi:10.1121/1.399855)
40. Strogatz SH. 2018 *Nonlinear dynamics and chaos: with applications to physics, biology, chemistry, and engineering*. Boca Raton, FL: CRC Press.
41. Pantaleone J. 2002 Synchronization of metronomes. *Am. J. Phys.* **70**, 992–1000. (doi:10.1119/1.1501118)
42. Guevara MR, Glass L, Shrier A. 1981 Phase locking, period-doubling bifurcations, and irregular dynamics in periodically stimulated cardiac cells. *Science* **214**, 1350–1353. (doi:10.1126/science.7313693)
43. Ermentrout GB, Rinzel J. 1984 Beyond a pacemaker's entrainment limit: phase walk-through. *Am. J. Physiol.-Regul., Integr. Comp. Physiol.* **246**, R102–R106. (doi:10.1152/ajpregu.1984.246.1.R102)
44. Néda Z, Ravasz E, Brechet Y, Vicsek T, Barabási AL. 2000 The sound of many hands clapping. *Nature* **403**, 849–850. (doi:10.1038/35002660)
45. Jones RM, Deng L, Leung K, McMahon D, O'Reilly MA, Hynynen K. 2018 Three-dimensional transcranial microbubble imaging for guiding volumetric ultrasound-mediated blood-brain barrier opening. *Theranostics* **8**, 2909–2926. (doi:10.7150/thno.24911)
46. Wu SY, Downs M, Sanchez CS, Teichert T, Buch A, Samiotaki G, Marquet F, Tung YS, Chen C, Ferrera V, Konofagou E. 2013 Monitoring of focused ultrasound-induced blood-brain barrier opening in non-human primates using transcranial cavitation detection in vivo and the primate skull effect. In *2013 IEEE International Ultrasonics Symposium (IUS)*, pp. 1201–1204. (doi:10.1109/ULTSYM.2013.0307).
47. Wu SY, Tung YS, Marquet F, Downs M, Sanchez C, Chen C, Ferrera V, Konofagou E. 2014 Transcranial cavitation detection in primates during blood-brain barrier opening–a performance assessment study. *IEEE Trans. Ultrason. Ferroelectr. Freq. Control* **61**, 966–978. (doi:10.1109/tuffc.2014.2992)
48. TS I *et al.* 2019 Measurement of cavitation noise in ultrasonic baths and ultrasonic reactors. In *IEC Technical Specification 63001*. International Electrotechnical Commission.
49. Eisener J *et al.* 2014 Correlation of cavitation bubble ensemble dynamics and acoustic emission spectra. In *Fortschritte der Akustik - DAGA 2014 Oldenburg* (ed. B Kollmeier), pp. 700–701. Berlin, Germany: Deutsche Gesellschaft für Akustik e.V. (DEGA).
50. Mettin R, Eisener J, Koch M, Holly D, Thiele M. 2024 On the sound emission of acoustic cavitation. In *Fortschritte der Akustik - DAGA 2024 Hannover* (eds J Peissig, R Rolfes), pp. 478–481. Berlin, Germany: Deutsche Gesellschaft für Akustik e.V. (DEGA).
51. Krefting D, Mettin R, Parlitz U, Lauterborn W. 2003 Akustische und räumliche Strukturbildung in Ultraschall-Kavitationsfeldern (Acoustic and spatial structure formation in ultrasonic cavitation fields). In *Fortschritte der Akustik - DAGA 2003* (ed. M Vorländer), pp. 832–833. Oldenburg, Germany: Deutsche Gesellschaft für Akustik e.V. (DEGA).
52. Masiello D, Tudela I, Shaw SJ, Jacobson B, Prentice P, Valluri P, Govindarajan R. 2024 Mass and heat transfer in audible sound driven bubbles. *Ultrason. Sonochem.* **111**, 107068. (doi:10.1016/j.ultsonch.2024.107068)
53. Metzger H, Zhang Y, Cammarano A, Prentice P. 2025 Revisiting the subharmonic route to acoustic chaos: broadband noise clearing via cavitation bubble synchronisation. Figshare. (doi:10.6084/m9.figshare.c.7874166)
54. Metzger H, Zhang Y, Cammarano A, Prentice P. 2025 Revisiting the subharmonic route to acoustic chaos: broadband noise clearing via cavitation bubble synchronization [Dataset]. (doi:10.5525/gla.researchdata.1668)